frontiers | Frontiers in Earth Science

TYPE Original Research
PUBLISHED 10 January 2023
DOI 10.3389/feart.2022.1033979

OPEN ACCESS

EDITED BY
Haikuan Nie,
SINOPEC Petroleum Exploration and Production Research Institute, China

REVIEWED BY
Zhaodong Xi,
China University of Geosciences, China
Subhashree Mishra,
Council of Scientific and Industrial Research (CSIR), India
Jianchao Cai,
China University of Petroleum, Beijing, China

*CORRESPONDENCE
Yuqi Huang,
sherrill-018@163.com
Jinchuan Zhang,
zhangjc@cugb.edu.cn

SPECIALTY SECTION
This article was submitted to Geochemistry, a section of the journal Frontiers in Earth Science

RECEIVED 01 September 2022
ACCEPTED 29 September 2022
PUBLISHED 10 January 2023

CITATION
Huang Y, Zhang J, Zhang P, Tang X and Yang J (2023), Multi-scale pore structure characteristics and main controlling factors analysis of Longtan formation shale in Northwest Guizhou. *Front. Earth Sci.* 10:1033979. doi: 10.3389/feart.2022.1033979

Multi-scale pore structure characteristics and main controlling factors analysis of Longtan formation shale in Northwest Guizhou

Yuqi Huang[1,2]*, Jinchuan Zhang[1]*, Peng Zhang[2], Xuan Tang[1] and Junwei Yang[2]

[1]School of Energy, China University of Geosciences (Beijing), Beijing, China, [2]School of Mining and Mechanical Engineering, Liupanshui Normal University, Liupanshui, China

Marine-continental transitional shale strata are widely distributed in China and have high gas potential. The Longtan shales are a typical marine-continental transitional coal-bearing shale system in Northwest Guizhou. Low-temperature N_2 adsorption experiments and high-pressure mercury injection experiments were carried out on the unweathered shale samples from Well JS-1. The multi-scale fractal dimensions were calculated based on the MESP (Menger-sponge) model, MESA (mercury saturation) model, and FHH (Frenkel-Halsey-Hill) model respectively. The macropores (≥100 nm) are mainly inorganic with a fractal dimension D1 between 2.8628–3.2057, indicating the macropore structure is relatively complex. The proportion of the macropores in total pores is not high in comparison to mini-micropores (<50 nm), and the content of brittle minerals and pyrite mainly controls its structure. Among the mesopores (50–100 nm), inorganic pores are still the primary pore type, but the proportion of organic pores increases. The fractal dimension D2 is between 2.2125–2.3016. It has medium complexity, and the proportion in the total pores is slightly higher than that of macropores. The influence of organic matter abundance on mesopore structure is greater than that in macropore because of the increase in the proportion of organic pores, making the controlling mechanism of mesopore structure more complicated. Mini-micro pores are mainly organic pores. The fractal dimension D3 (fractal dimension of mini-micropores under low relative pressure, P/P_0 ≤0.5) ranges between 2.6709–2.8648, and D3′ (fractal dimension of mini-micropores under high relative pressure, P/P_0 >0.5) ranges between 2.6661–2.9256, indicating complex pore structures and rough surfaces. Mini-micropore accounts for the highest proportion of the total pores and its structure is mainly controlled by the abundance of organic matter. The pore structures of macropores and mesopores greatly influence the proportion of desorption gas in shale, while the structure of mini-micropores can control the maximum adsorbed gas volume of shale.

KEYWORDS

Northwest Guizhou, Longtan formation, pore structure of shale, fractal characteristics, gas content

1 Introduction

Shale gas is an unconventional natural gas resource mainly stored in free and adsorbed states in shale strata (Yang et al., 2013a; Xiao et al., 2013; Yang et al., 2014; Chen et al., 2021; Zhang et al., 2021). After more than a decade of exploration and development, China's shale gas research has made numerous breakthroughs, but most are concentrated in the marine shale strata in Sichuan Basin. Marine-continental transitional shales have a wide distribution in China and have excellent exploration potential, but their reservoir characteristics are complex, determining the necessity of quantitatively and finely studying the reservoir characteristics.

The pore structure is an important field of reservoir research. It mainly conducts qualitative or quantitative research on the type, shape, size distribution, complexity, and heterogeneity of pores (Chen et al., 2005; Ross and Bustin, 2009; Zhang et al., 2015; Shao et al., 2017; Zhang et al., 2018; Liu and Ostadhassan, 2019; Wood, 2021; Xie et al., 2022). Qualitative research on shale pore structure mainly relies on high-resolution image analysis technology, such as FE-SEM (field emission scanning electron microscopy), FIB-SEM (focused ion beam scanning electron microscopy), TEM (transmission electron microscopy), and CT (computed tomography). Loucks et al. used FE-SEM to study Barnett shale in the Forth Worth basin, and believed that the matrix-related pore network in mudrocks was composed of nanometer-to micrometer-size pores, and dominated by organic matter pores (Loucks et al., 2012; Loucks and Reed, 2014). Sun et al. (2016) used FIB-SEM to conduct 3D (three dimension) imaging of the shale of the Longmaxi Formation in the Sichuan Basin and the carbonate rock of the Lucaogou Formation in the Junggar Basin. Guo et al. and Bai et al. studied the shale and tight sands of the Yanchang Formation in the Ordos Basin, using nano-CT technology, and obtained the 3D distribution characteristics of pores Bai et al. (2013), Guo et al. (2015). Quantitative research mainly relies on experiments and calculations. Ross et al. conducted gas adsorption experiments and mercury injection experiments on Devonian and Jurassic shale in the Western Canadian Sedimentary Basin, and believed that inorganic minerals (especially clay minerals) influenced modal pore size, total porosity and sorption characteristics of shales (Ross and Bustin, 2009). Clarkson et al. studied geometry, size distribution, connectivity, and other characteristics of pores of the typical shale reservoirs in North America through experiments such as gas adsorption and high-pressure mercury injection (Clarkson et al., 2012). Chalmers et al. studied the Cretaceous shale in northeastern British Columbia through gas adsorption experiments and believed that shales with higher SSA (specific surface area) had higher methane sorption capacities, and TOC (total organic carbon) content was the most significant control on methane sorption capacity, however, other important factors included the kerogen type, maturity, and clay content, in particular the abundance of illite (Chalmers and Bustin, 2008). Tian et al. (2012) studied the pore structure of shales in the Sichuan Basin and the Bohaiwan Basin, by using gas adsorption and high-pressure mercury injection experiments. They believed that the development of pores larger than 50 nm was mainly related to the content of inorganic minerals such as clay minerals, while the development of pores smaller than 50 nm was mainly related to the abundance of organic matter. After studying the marine shale of the Longmaxi Formation in the Sichuan Basin, Zhu et al. believed that pores smaller than 2 nm contributed little to the total pore volume of the reservoir, and the oil and gas flow (Zhu et al., 2016).

In recent years, fractal theory has been applied to the study of shale pore structure. The fractal dimension is a quantitative parameter that can effectively describe the irregularity of complex objects. Scholars regard shale as an irregular porous medium and use fractal dimension to quantitatively characterize the irregular pores in shale (Yang et al., 2014; Zhang et al., 2016; Shao et al., 2017; Zhang et al., 2018; Liu and Ostadhassan, 2019; Huang et al., 2020; Wood, 2021; Xie et al., 2022). Yang et al. (2014) conducted N_2 adsorption experiments on the Niutitang shales in the Sichuan Basin and calculated the fractal dimension based on the FHH (Frenkel-Halsey-Hill) model. Their research showed that the fractal dimension of the Niutitang shales was large, indicating strong heterogeneity of shale pores. The fractal dimension showed a positive correlation with TOC and negative correlations with porosity and permeability. The higher the fractal dimension, the more complicated the pore structure, which was favorable for gas adsorption but unfavorable for gas flow. Zhang et al. (2016) studied the pore structure of Taiyuan Formation shale in the eastern uplift of the Liaohe Depression based on mercury injection experiments and calculated the fractal dimension based on the MESP (Menger-sponge) model. Results showed that the fractal dimension of Taiyuan shales was close to 3, indicating the strong heterogeneity of pores. The fractal dimension had a poor correlation with TOC, a strong negative correlation with clay minerals, and a weak positive correlation with quartz content. After summarizing the previous research, it is not difficult to see that most scholars agree that the larger the fractal dimension is, the more complex the pore structure is, and the complex pore structure is not conducive to gas flow. However, there is no consensus on the main controlling factors of pore structure and the impact of pores with different sizes on gas storage capacity. Some scholars have noticed that different experiments and calculation models could cause different results for the same pore structure problem (Wood, 2021; Xie et al., 2022). Therefore, it is very important to select and use effective pore classification standards and suitable experiments and calculation models when studying the pore structure of shale with large pore size distribution and multiple pore types such as marine-continental transitional shale.

This paper selected the Longtan shales, typical marine-continental transitional facies shale strata in northwest Guizhou, China, which has great gas content and is considered one of the non-marine shales most likely to

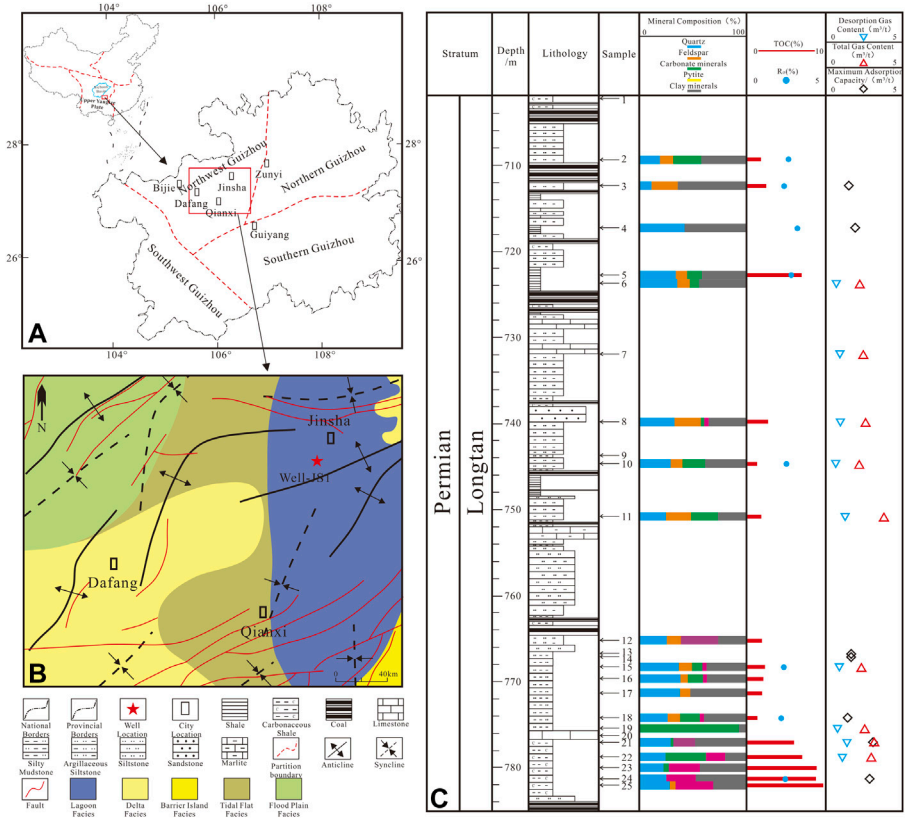

FIGURE 1
Geological background (Su, 2014; Feng, 2020; Huang et al., 2020) and sampling information of Well JS-1 [**(A)** location of the study area; **(B)** regional sedimentary facies and structures and well location; **(C)** sample and geological conditions of Well JS-1].

achieve a breakthrough, as the research target. High-pressure mercury injection and low-temperature N_2 adsorption experiments are comprehensively used to study the structure of pores with different apertures. Based on the MESP model, MESA (mercury saturation) model, and FHH model, the fractal dimensions are calculated to form the comprehensive characteristics of the multi-scale pore structure of the Longtan shales in northwest Guizhou. Further studies are conducted to clarify the main controlling factors of multi-scale pore structure and their effects on shale gas-bearing characteristics, hoping to provide theoretical support for the reservoir evaluation and the gas development of the marine-continental transitional shale gas resources.

2 Materials and methods

2.1 Materials

Twenty-five samples were used consisting of unweathered drilled core samples from well JS-1, with a depth range of 702–782 m (Figure 1). A comprehensive experimental procedure was conducted for these samples, including TOC (total organic carbon) content tests, XRD (x-ray diffraction) analyses of mineral composition, low-temperature N_2 adsorption experiments, high-pressure mercury injection experiments, gas content tests, and isothermal adsorption experiments.

2.2 Experimental methods

TOC content was measured using a LecoCS230 analyzer. The homogenized powder samples (<0.2 mm) were treated with 5% hydrochloric acid at 80°C to remove inorganic carbon. The samples were rinsed with pure water to remove residual acid until the pH reached neutral. After drying, the processed samples were placed into the apparatus to measure TOC content. The experiments conformed to the national standard GB/T19145-2003 of China.

The mineralogical composition was measured using an X'Pert Powder X-ray diffractometer with 40 kV and 40 mA.

Powder samples (200–300 mesh) were rinsed with chloroform to remove the organic matter and dried in an oven at 60°C until the weight remained unchanged before XRD analysis. The experiments conformed to the industry standard SY/T5163-2010 of China.

High-pressure mercury injection experiments were performed using an Auto Pore IV9500 Automatic Mercury Porosimeter. The samples (1 cm^3 cube) were placed in a drying oven and dried for 24 h at 60°C. They were then removed and cooled to room temperature. Then, mercury injection experiments were conducted under pressures ranging from 0 to 215 MPa. The experiments conformed to the national standard GB/T21650.1-2008 of China.

Low-temperature N_2 adsorption experiments were performed using a Quadrasorb SI specific surface analyzer. The powder samples (≤80 mesh) were dried for 24 h at 150°C in an oven and high vacuum degassed for 4 h at 90°C. Then, N_2 adsorption experiments were conducted under a relative ranges of 0.040–0.997. The experiments conformed to the national standard GB/T19587-2004 of China.

The maximum adsorption capacity was measured using a GAI-100 high-pressure gas isothermal adsorption apparatus with a pressure range of 0.007–17.300 MPa at 30°C. The experiment conformed to the industry standard SY/T 6132–1995 of China.

The gas content was measured using a tubeless field desorption instrument and a fully sealed residual gas analyzer developed by the China University of Geosciences (Beijing). Desorbed gas content and residual gas content data were obtained by these equipments, and the lost gas content was obtained by calculation based on the ISO18871-2015.

2.3 Analysis methods

2.3.1 Menger-sponge model

MESP model was first proposed by Menger, K. in 1928 (Menger, 1928). It is a general fractal calculation curve with a topological dimension of 1. According to this theory, any curve is homeomorphic to a subset of MESP. This model was widely used in the quantitative study of pore structure of coal (Fu et al., 2007; Zhang et al., 2016). The general model is simplified as:

$$D = 4 + \frac{\ln(dV_p/dP)}{\ln P} \tag{1}$$

where D—the fractal dimension, unitless; V_p—the volume of the pore, cm^3/g; P—the pressure, MPa.

2.3.2 Mercury saturation model

In the actual fractal dimension calculation, it can be seen that when the aperture is less than 100 nm, the linear relationship between the MESP model calculation data is not very good (Fu et al., 2007; Zhang et al., 2016; Liu, 2020). Therefore, the saturation model is used to supplement the MESP model in this study.

The saturation model can be divided into a WASA (water saturation) model and a MESA model. Previous studies have shown that the fractal dimension calculation results of the MESA model have a good characterization effect on pore structure. In contrast, the fractal dimension calculation results of the WASA model have a low correlation with pore structure parameters (Lai et al., 2013; Deng et al., 2018). Therefore, the capillary bundle fractal formula based on MESA (Cheng et al., 2022) is used to calculate and analyze mercury injection data in this paper:

If the pore distribution of rocks conforms to fractal characteristics, the relationship between pore number N (>r) and pore radius r is consistent:

$$N(>r) = ar^{-D} \tag{2}$$

where: aa constant; D—the fractal dimension, unitless.

The pore number N (>r) also conforms to the relationship:

$$N(>r) = \frac{V_{Hg}}{r^2 l\pi} \tag{3}$$

where: V_{Hg}—the cumulative injection mercury volume, cm^3; l—the capillary length, cm.

Combining the above two equations with the Laplace equation:

$$S_{Hg} = bP_c^{-(2-D)} \tag{4}$$

where: S_{Hg}—the mercury saturation, %; b—a constant; P_c—the pressure, MPa.

Taking the logarithms on both sides of the equation gives:

$$\ln S_{Hg} = (D-2)\ln P_c + \ln b \tag{5}$$

2.3.3 Frenkel-Halsey-Hill model

Pfeiferper proposed the FHH model in 1983 (Pfeiferper and Avnir, 1983), also known as FHH thick plate theory. This model is based on the gas adsorption data to calculate the fractal dimension of the solid porous medium, which is widely used in the study of shale pore structure (Shao et al., 2017; Zhang et al., 2018; Wood, 2021; Xie et al., 2022). The simplified equation is:

$$\ln V = k + (D-3)ln[ln(P_0/P)] \tag{6}$$

where k—a constant; V—the volume of adsorbed gas, cm^3/g; P_0—the saturated vapor pressure, MPa; P—the equilibrium pressure, MPa; D - the fractal dimension, unitless.

2.3.4 Correlation analysis

Because there are dimensional differences among parameters, the order of magnitude of the value of each parameter is different. Correlation analysis without any pretreatment may affect the accuracy of results. Therefore, all parameters should be made dimensionless before correlation analysis. The threshold method is

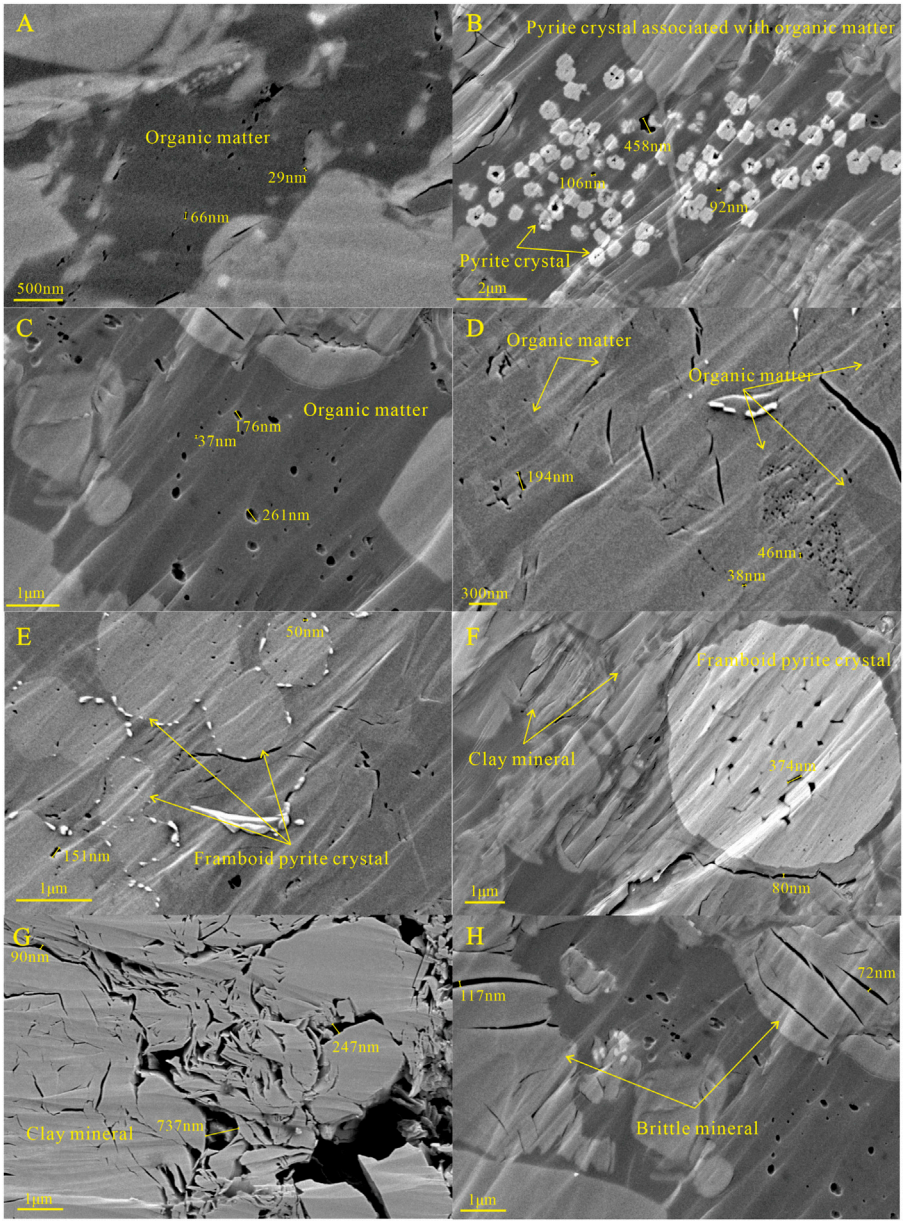

FIGURE 2
Argon ion polishing FE-SEM photographs of Longtan shales (Zhang et al., 2018; Huang et al., 2020). **(A)**. 751.04 m, silty mudstone, ellipsoidal organic pores developed, mainly mini-mesopores; **(B)**. 781.42 m, carbonaceous shale, pyrite crystal associated with organic matter, microfractures developing around granules; **(C)**. 781.42 m, carbonaceous shale, spherical organic pores developed, mostly meso-macropores; **(D)**. 779.27 m, carbonaceous shale, honeycomb, and quasi-honeycomb organic pores developed, mostly mini-micropores; **(E)**. 779.27 m, carbonaceous shale, intercrystalline pyrite pores developed inside the framboid pyrite crystal, from minipore to macropores can be observed, microfractures developed at the edge of granules; **(F)**. 781.42 m, carbonaceous shale, intercrystalline pyrite pores developed inside the framboid pyrite crystal, microfractures can be observed; **(G)**. 709.34 m, carbonaceous shale, clay minerals are stratiform and flaky shaped, intercrystalline clay mineral pores developed; **(H)**. 781.42 m, carbonaceous shale, microfractures developed in brittle mineral granules).

used in this paper to eliminate the order of magnitude differences between parameters. The equation is:

$$y_i = \frac{x_i - x_{\min}}{x_{\max} - x_{\min}} \quad (7)$$

where y_i—the dimensionless value; x_i—the original value; x_{max}—the original maximum value of the parameter series; x_{min}—the original minimum value of the parameter series.

The correlations between fractal dimensions and geological parameters are analyzed by SPSS software (International

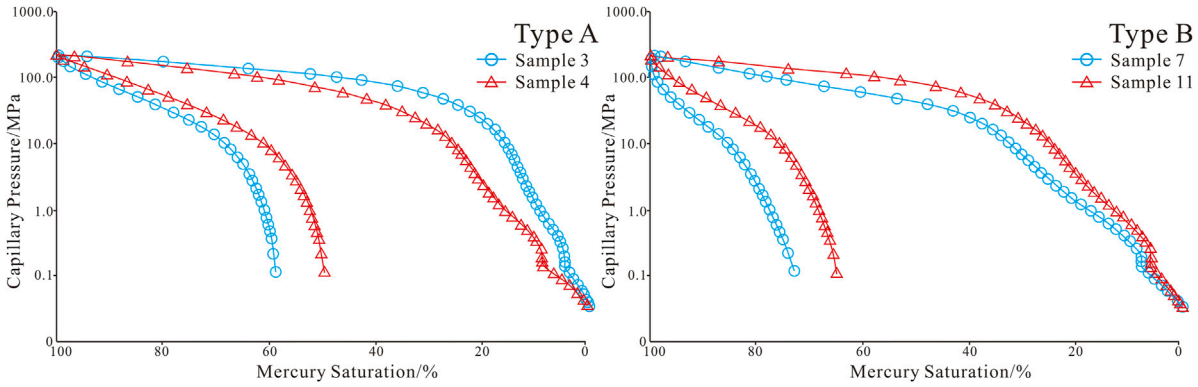

FIGURE 3
Mercury injection-ejection curve.

Business Machines Corp). Pearson correlation coefficient (applicable to quantitative data obeying normal distribution) and Spearman correlation coefficient (applicable to data of various distribution forms and sample sizes) are selected for correlation analysis. The smaller the significance value of the correlation coefficient, the stronger the correlation. When the significance is less than 0.05, the two variables have a significant correlation (Su, 2021).

3 Geological setting

The study area is in northwest Guizhou Province, China. It is located in the Qianzhong Uplift and the box fold belt in the Dianqianbei depression on the Upper Yangtze plate (Huang et al., 2020; Su, 2014; Feng, 2020; Deng et al., 2022; Bureau of Geology and Mineral Exploration and Development Guizhou Province, 1987). Folds and faults are significantly developed in the region. Folds mainly strike in NE to NNE direction (Su, 2014; Feng, 2020; Deng et al., 2022). Faults formed under the mutual cutting, combination, and interference of multiple trending faults, mainly in NE and NNE directions. The Dongwu movement at the turn of the early and late Permian led to the widespread closure of the upper Yangtze platform basin and uplift. Northwest Guizhou was a coastal zone where sea and land alternated. Lagoonal, tidal delta facies, tidal flat, and peat swamp facies are widespread throughout the Longtan Formation (Bureau of Geology and Mineral Exploration and Development Guizhou Province, 1987), forming a set of coal-bearing shale strata with numerous layers and enormous cumulative thicknesses. The primary lithology of the Longtan Formation are carbonaceous shale, silty mudstone, argillaceous siltstone, siltstone, marlstone, and coal (Figure 1). The macerals of kerogen are mainly vitrinite, and the organic matter type index is −12 to −78, indicating that the organic matter of Longtan shales is all type III kerogen (Zhang et al., 2018; Huang et al., 2020). The distribution range of TOC content ranges from 1.36% to 9.58% (Figure 1), and the overall organic matter abundance is high (Huang et al., 2020; Deng et al., 2022). Ro (vitrinite reflectance) value is distributed between 2.0%–3.0%, indicating that the organic matter in the Longtan shales is in the early overmature stage (Huang et al., 2020). According to the organic geochemical parameters, the Longtan shales in Northwest Guizhou have good gas generation conditions. XRD mineral and clay analysis results show that the Longtan shales are mainly composed of quartz, feldspar, carbonate minerals, and clay minerals. The quartz contents range from 0.00%–41.80%, with an average of 27.26%. Clay minerals comprise the remaining 0.005–64.30%, with an average of 38.61%, which is relatively high (Figure 1). The clay minerals mainly consist of illite/montmorillonite and illite, with minor chlorite, kaolinite, and smectite (Huang et al., 2020; Deng et al., 2022).

4 Results

4.1 Pore classification and morphological characteristics

The scientific size classification of pores is the basis of this multi-scale study. In the field of coal geology, the pores in coal are often divided into micropores (<10 nm), minipores (10–100 nm), mesopores (100–1,000 nm), and macropores (≥1,000 nm) according to the Huoduote decimal classification standard. In the field of unconventional gas geology (Xoaotb et al., 1966; Fu et al., 2007; Yang et al., 2013b), shale pores are often divided into micropores (<2 nm), mesopores (2–50 nm), and macropores (≥50 nm) according to the IUPAC (International Union of Pure and Applied Chemistry) pore division scheme (Rouquerol et al., 1994; Shao et al., 2017;

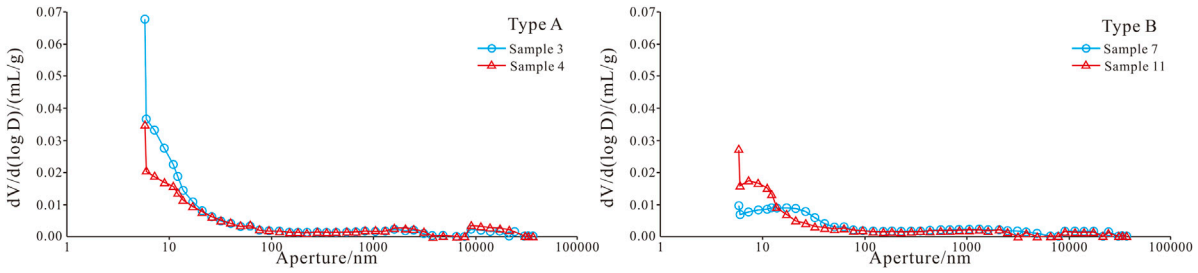

FIGURE 4
Aperture distribution curve based on the high-pressure mercury injection experiments.

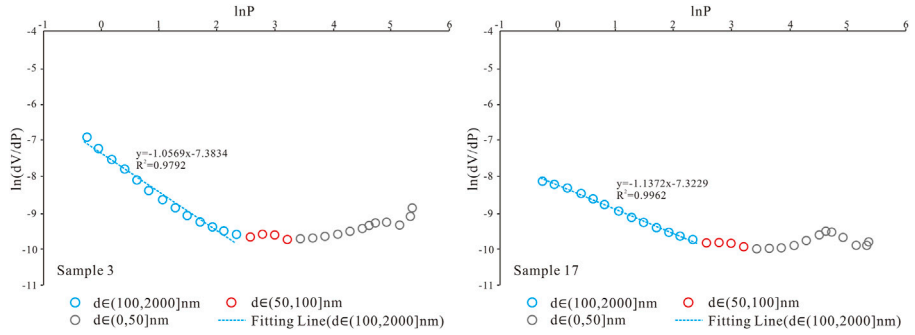

FIGURE 5
Fractal dimension calculation based on the MESP model.

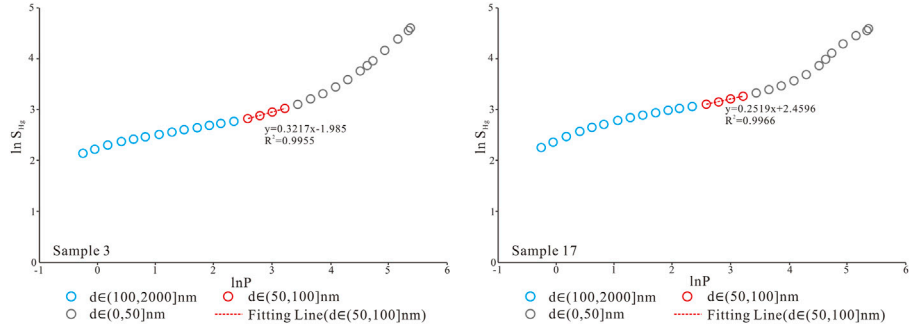

FIGURE 6
Fractal dimension calculation based on the MESA model.

Zhang et al., 2018; Liu and Ostadhassan, 2019; Huang et al., 2020; Xie et al., 2022). By comparing these two classification schemes, it can be seen that the Huoduote classification covers all sizes of pores, while the IUPAC division scheme focuses more on the study of smaller pores. The Longtan shales are a set of coal-bearing strata of marine-continental transitional facies, which have both coal and shale characteristics and a wide range of pore size distribution. If the IUPAC pore division scheme is used alone, the classification of large pores would be too rough for refined research. Therefore, the IUPAC division scheme and Huoduote classification were combined in this paper to divide the pores of Longtan shales into micropores (<2 nm), minipores (2–50 nm), mesopores (50–100 nm), and macropores (≥100 nm).

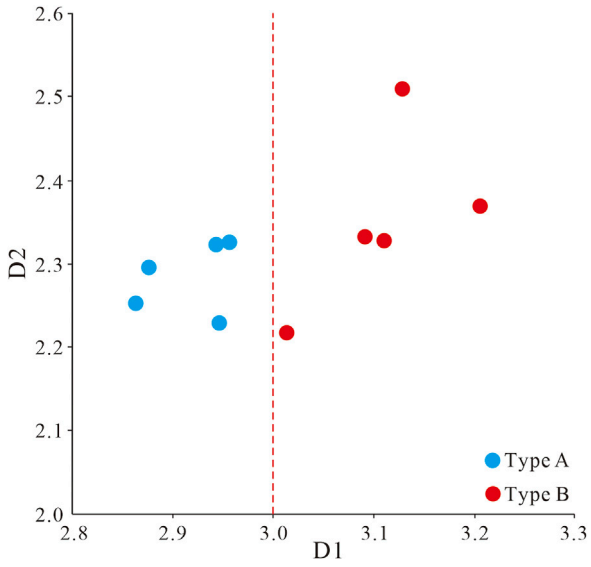

FIGURE 7
Fractal dimension of macropores and mesopores of Longtan shales.

The pore micromorphology can be observed by Argon ion polishing FE-SEM (Figure 2). According to the development place and morphological characteristics, the pores of Longtan shales can be divided into organic pores (developed in organic granules), inorganic pores (developed in inorganic mineral granules), and microfractures. Spherical and ellipsoidal organic pores have poor connectivity and relatively smooth surfaces and range in size from minipores to macropores (Figures 2A–C). Honeycomb and quasi-honeycomb organic pores have good connectivity and small aperture, most of which are mini-micropores (Figure 2D). The most common inorganic pores are intercrystalline pyrite pores and intercrystalline clay mineral pores. Intercrystalline pyrite pores commonly develop inside the framboid pyrite crystal, mostly ink bottle or irregular shaped. The intercrystalline pyrite pores are mostly mesopores and minipores, and macropores can also be observed (Fig. B, E, and F). Clay mineral crystals are mostly flaky, scaly, and filiform, which determines that the intercrystalline clay mineral pores are mostly slit-shaped and wedge-shaped, with pore sizes ranging from micropores to macropores (Figure 2G). Intragranular and around-granule fractures are the primary microfractures in the Longtan shales (Loucks et al., 2012; Yang et al., 2013a; Loucks and Reed, 2014). The former is mainly developed in brittle minerals (Figure 2H), and the latter is at the edge of granules (Figures 2A,E). The width of microfractures varies greatly, ranging from nanoscale to milliscale.

4.2 Pore structures

4.2.1 High-pressure mercury injection experiment analysis

A high-pressure mercury injection experiment can theoretically study the pores with apertures ranging from 5 nm to 1,000 μm. But in the actual test process, the structures of pores with small apertures are easily damaged in the process of mercury injection, resulting in significant errors in the characterization of micro-minipore structure (Qin et al., 2020; Xu, 2021). In addition, the test data of this study show that when the aperture is greater than 2000 nm, both the mercury injection-ejection curve and the aperture distribution curve have abnormal bending to varying degrees. Therefore, this paper only uses high-pressure mercury injection experiment data to analyze the structural characteristics of mesopores and macropores less than 2000 nm.

The Longtan shales can be divided into two types of shales (Figure 3) according to the shape of the mercury injection-ejection curve and the mercury ejection efficiency based on the high-pressure mercury injection experiments (Yang et al., 2013b; Liu et al., 2021).

Type A: when the injection pressure reaches 20 MPa, the mercury volume increases significantly. The injection curve

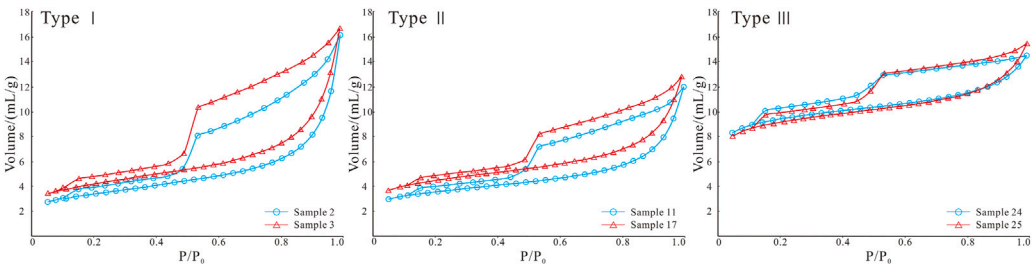

FIGURE 8
N_2 adsorption-desorption curves.

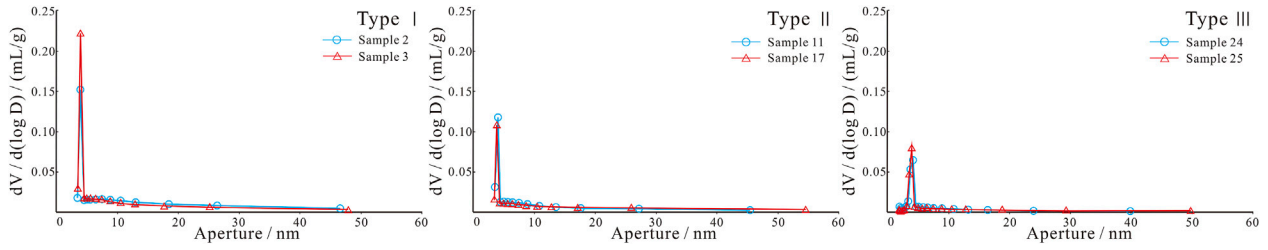

FIGURE 9
Aperture distribution curve based on the low-temperature N_2 adsorption experiments.

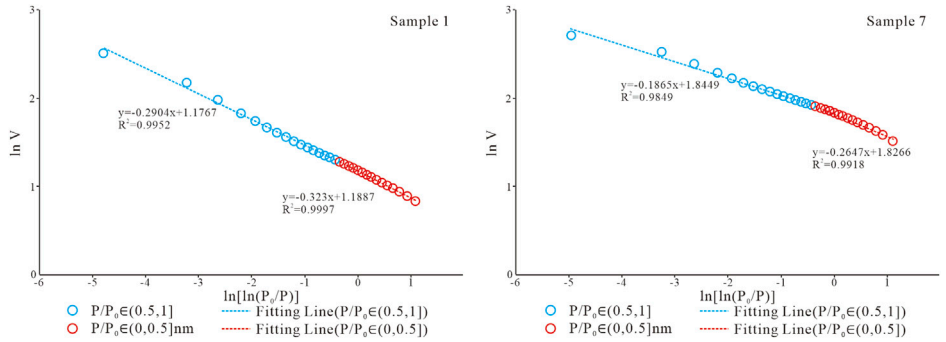

FIGURE 10
Fractal dimension calculation based on the FHH model.

within the range of 20–215 MPa (corresponding to the aperture range of 5–50 nm) is nearly horizontal, and the corresponding mercury volume accounts for about 70%–80% of the total injection mercury volume (Figure 3). The aperture distribution curve presents a single peak shape. The main peak is at 5nm, then gradually decreases within the 5–100 nm aperture range (Figure 4). The mercury ejection efficiency is 40%–60%. This shows that micro-minipores are highly developed in type A rocks, followed by mesopores, with general connectivity and complex structure (Tu et al., 1983; Tang and Zeng, 1994; Yang et al., 2013a).

Type B: when the injection pressure reaches 20 MPa, the mercury volume increases significantly. The mercury volume between 20 and 215 MPa accounts for 50%–70% of the total mercury injection volume (Figure 3). The aperture distribution curve presents a double peak shape, with peaks at about 5 nm and 10–50 nm, respectively (Figure 4). The mercury ejection efficiency is 20%–40%. It shows that, compared with type A, the proportion of micro-minipores in type B rocks decreases while the proportion of meso-macropores increases. Overall, the pore structure is more complex than type A rocks.

The curve shape has prominent segmentation characteristics. The fitting line fits well when the aperture is within 100–2,000 nm. There is no good linear relationship when the aperture is less than 100 nm (Figure 5). Therefore, the MESP model is used to calculate the fractal dimension of macropores with apertures of 100–2,000 nm, which is recorded as D1. The results show that D1 values are between 2.8628–3.2057, with an average value of 3.0132. The overall D1 values of the Longtan shales are relatively large, reflecting the complex macropore structure. This is because, under the influence of tectonism, a microfracture network easily develops within the highly brittle minerals within the rocks. Coupled with the clay mineral intercrystalline pores, the macropores present a state of complex structure and rough surface.

In the log-log graph, the curve of the mesopores zone is approximately a straight line. The fitting line fits well (Figure 6), and the fractal dimension of the mesopores calculated based on the MESA model is recorded as D2. The results show that the D2 value is between 2.2125–2.3016, with an average of 2.2504, reflecting that the mesopore complexity is medium. This is because mesopores' proportion of intercrystalline pyrite and

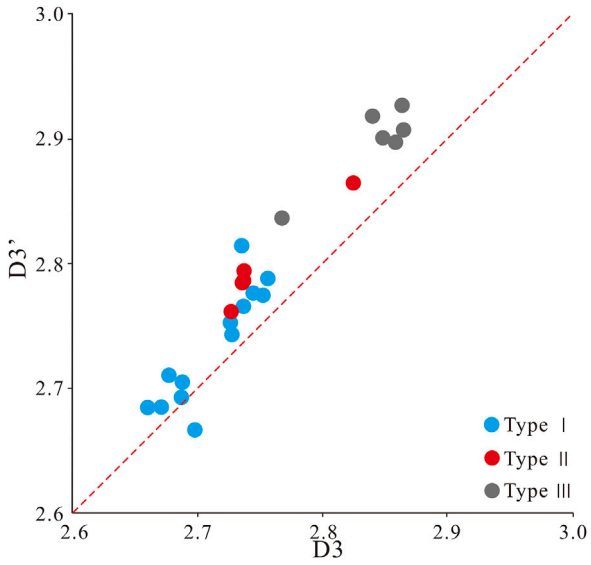

FIGURE 11
Fractal dimension of micro-minipores of Longtan shales.

spherical-ellipsoidal organic pores increases. These two types of pores have relatively simple structures and smooth pore surfaces, resulting in relatively low fractal dimensions of mesopores.

Overall, for type A shales, D1 and D2 are relatively small, and D1 is less than 3.00, while D2 is less than 2.35. For type B shales, D1 is significantly greater than type A, all of which are greater than 3.00. D2 is slightly larger than type A, mostly larger than 2.30. The results show that the macropores and mesopores structures of type B rocks are more complex than that of type A (Figure 7).

4.2.2 Low-temperature N_2 adsorption experiment analysis

The low-temperature N_2 adsorption experiments can characterize pore structure with a nanoscale aperture (0.35–200 nm) (Yang et al., 2013b; Qin et al., 2020). Therefore, the low-temperature N_2 adsorption experiment was used to study the micro-minipore characteristics in this paper.

Compared to the N_2 adsorption-desorption curves with the IUPAC (2015) classification standard (Liu et al., 2005; Cheng et al., 2022), the Longtan shales can be divided into three types (Figures 8, 9).

Type I has a typical H2 (a) -H3 hysteresis loop. The adsorption curve does not have a horizontal segment in the sizeable relative pressure zone but has steep desorption branches, reflecting that there are abundant flaky granules in the rock. The pores are mainly slit-shaped and wedge-shaped, and some ink bottle-shaped pores. The aperture distribution curve presents a single peak shape, with the peak at 2–5 nm.

Type II is characterized by the H3 type hysteresis loop, which is narrower than type I, reflecting that the flaky and stratiform granules in the rock are extensively developed. The pores are mainly slit-shaped and wedge-shaped. The aperture distribution curve also has a single peak at 2–5 nm, but the height is lower than type I, reflecting that the proportion of minipores is lower than type I.

Type III is characterized by the H3-H4 hysteresis loop, with an adsorption curve close to the horizontal and narrow hysteresis loop. There is adsorption volume in the low relative pressure zone, indicating the existence of micropores. The pores are mainly slit-shaped, with significant aperture differences. The peak height at 2–5 nm is the lowest, reflecting that the proportion of minipores is the lowest.

The fractal dimensions calculated based on the low-temperature N_2 adsorption experiment data and the FHH model can well characterize the gas adsorption and storage capacity and complexity of pores (Chen et al., 2021; Zhang et al., 2018; Bureau of Geology and Mineral Exploration and Development Guizhou Province, 1987). The curve shows a segmented feature in the log-log graph (Figure 10), and the piecewise fitting lines reflect two different fractal dimensions of one sample. The fractal dimension recorded as D3 of the low relative pressure zone ($P/P_0 \leq 0.5$) can adequately characterize the adsorption and gas storage capacity of the rock. The fractal

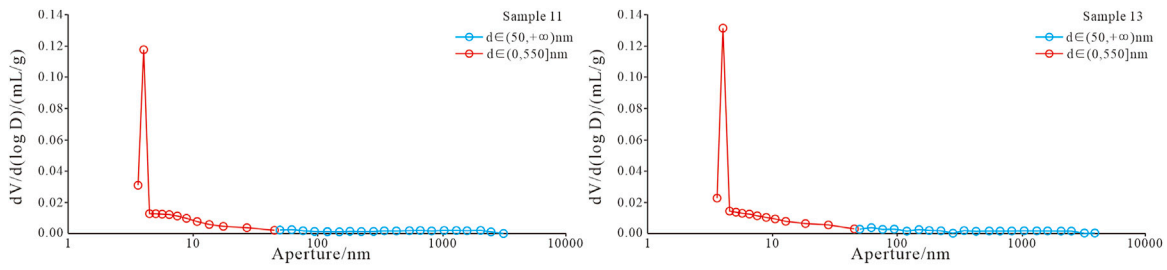

FIGURE 12
Multi-scale analysis of aperture distribution of Longtan shales.

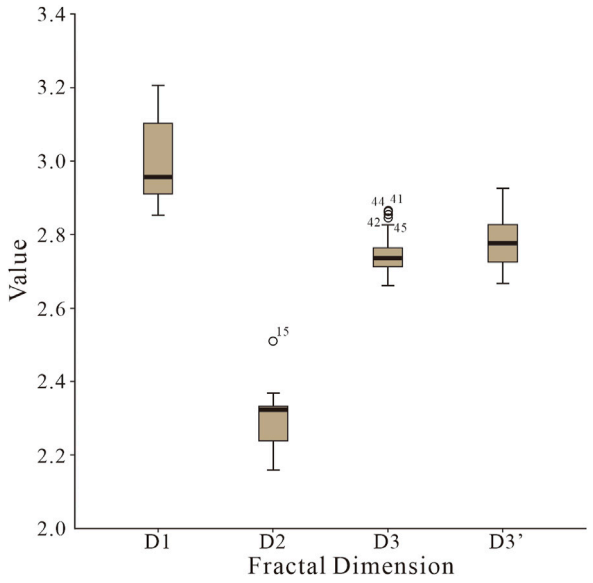

FIGURE 13
Box plot of fractal dimension multi-scale calculation results.

dimension recorded as D3′ of the high relative pressure zone (P/P_0 >0.5) can characterize the roughness and complexity of the pore. D3 ranges between 2.6709–2.8648, with an average value of 2.7489. D3' ranges between 2.6661–2.9256, with an average value of 2.7836. The overall values are close to 3, reflecting that the micro-minipores of the Longtan shales have complex structures and rough surfaces.

Overall, the D3 and D3′ of the type I shales are relatively low, indicating the pore structure of type I is relatively simple. The majority of the D3′ values are larger than D3. The D3 and D3′ of type II shales are slightly larger than that of type I, indicating the pore structure is slightly more complex than type I pores. The D3 and D3′ of type III shales are the largest, indicating the pore structures of the type III shales are the most complex among the three types. The D3' values of type II and type III shales are larger than D3 (Figure 11).

4.3.3 Multi-scale analysis

Combining the aperture distribution results of the high-pressure mercury injection experiments with that of the low-temperature N_2 adsorption experiments (Figure 12), the aperture distribution of Longtan shales shows a typical single peak shape, with the peak located at 2–5 nm. The pore volume of 5–50 nm gradually decreases, and a very slight increase in the range of 50–100 nm can be observed. Indicating that micro-minipores contribute significantly to the total pore volume of the Longtan shales. The overall proportion of mesopores is not high in comparison to mini-micropores, and the proportion of macropores is the lowest.

The box plot of the fractal dimension multi-scale calculation (Figure 13) shows that: the D1 value of Longtan shales has a relatively scattered and right-skewed distribution, with the median value close to 3.00; therefore no abnormal values. The dispersion of the D2 value is moderate, with a left-skewed distribution and a mild outlier. The D3 value shows a centralized distribution, essentially obeying the normal distribution, with four mild outliers. D3' value has a moderate dispersion, essentially obeying a normal distribution, and there is no abnormal value. Considering the heterogeneity of the Longtan shales, and the pore fractal dimension is controlled by geological conditions such as mineral composition and organic geochemical conditions (Zhang et al., 2018; Xie et al., 2020; Zhang et al., 2020; Cheng et al., 2022; Xu et al., 2022), it is reasonable and acceptable that there are a few mild outliers in D2 and D3. Thus, it is unnecessary to delete these outliers; all the fractal dimension values can be used for follow-up analysis and calculation.

5 Discussions

5.1 Main controlling factors of multi-scale fractal dimensions

The results show various correlations between the fractal dimensions of pores at different scales (Table 1). D1 has a significant positive correlation with D2, but no significant correlation with D3 and D3', indicating that the favorable conditions for the development of macropores are similar to mesopores. However, there seems to be no relationship to the developmental conditions of mini-micropores.

D1 has a significant negative correlation with clay mineral content, a positive correlation with pyrite content, a generally positive correlation with carbonate mineral content and feldspar content, and no correlation with TOC content and quartz content (Figure 14). This indicates that the macropores in the Longtan shales are mainly inorganic pores controlled by the total content of brittle minerals and pyrite.

The correlation between D2 and the main factors is similar to D1, but the correlation significance with inorganic minerals decreases, while the correlation significance with TOC content increases (Figure 14). This is due to the increase in the proportion of organic pores in the mesopores of Longtan shales.

The D3 and D3' of the Longtan shales have a significant positive correlation with TOC content and pyrite content and a significant negative correlation with feldspar content (Figure 14). This is because the mini-micropores are mainly honeycomb and quasi-honeycomb organic pores, with complex pore structures and rough pore surfaces.

TABLE 1 The correlation analysis results of the fractal dimensions and different parameters.

		D1	D2	D3	D3′	TOC content	Clay mineral content	Quartz content	Carbonate mineral content	Feldspar content	Pyrite content
D1	Pearson	1.000 (–)									
	Spearman's rho	1.000 (–)									
	Number	10									
D2	Pearson	0.602 (0.065)	1.000 (–)								
	Spearman's rho	0.721 (0.019)	1.000 (–)								
	Number	10	10								
D3	Pearson	0.151 (0.721)	0.118 (0.781)	1.000 (–)							
	Spearman's rho	0.167 (0.693)	0.167 (0.693)	1.000 (–)							
	Number	8	8	23							
D3′	Pearson	0.027 (0.949)	0.268 (0.521)	0.962 (0.000)	1.000 (–)						
	Spearman's rho	0.048 (0.911)	0.262 (0.531)	0.922 (0.000)	1.000 (–)						
	Number	8	8	23	23						
TOC	Pearson	0.287 (0.640)	0.814 (0.094)	0.838 (0.000)	0.812 (0.000	1.000 (–)					
	Spearman's rho	0.200 (0.747)	0.700 (0.188)	0.671 (0.006)	0.661 (0.007)	1.000 (–)					
	Number	5	5	15	15	16					
Clay Mineral content	Pearson	−0.753 (0.051)	−0.160 (0.733)	−0.032 (0.898)	−0.018 (0.945)	−0.054 (0.844)	1.000 (–)				
	Spearman's rho	−0.821 (0.023)	−0.464 (0.294)	−0.042 (0.868)	0.038 (0.880)	0.057 (0.833)	1.000 (–)				
	Number	7	7	18	18	16	19				
Quartz Content	Pearson	−0.228 (0.624)	−0.207 (0.657)	0.090 (0.722)	0.107 (0.671)	−0.089 (0.742)	0.436 (0.062)	1.000 (–)			
	Spearman's rho	−0.500 (0.253)	−0.250 (0.589)	0.036 (0.887)	−0.013 (0.958)	−0.068 (0.803)	0.260 (0.283)	1.000 (–)			
	Number	7	7	18	18	16	19				
Carbonate Mineral Content	Pearson	0.429 (0.337)	0.189 (0.685)	−0.197 (0.432)	−0.224 (0.371)	−0.213 (0.429)	−0.775 (0.00)	−0.642 (0.003)	1.000 (–)		
	Spearman's rho	0.741 (0.057)	0.259 (0.574)	−0.062 (0.807)	−0.102 (0.687)	−0.402 (0.123)	−0.543 (0.016)	−0.322 (0.179)	1.000 (–)		
	Number	7	7	18	18	16	19	19	19		
Feldspar Content	Pearson	0.701 (0.079)	0.576 (0.176)	−0.551 (0.018)	−0.533 (0.023)	−0.675 (0.004)	0.163 (0.506)	−0.013 (0.957)	−0.206 (0.397)	1.000 (–)	
	Spearman's rho	0.571 (0.180)	0.643 (0.119)	−0.445 (0.064)	−0.496 (0.036)	−0.581 (0.018)	−0.079 (0.747)	−0.064 (0.794)	−0.008 (0.974)	1.000 (–)	
	Number	7	7	18	18	16	19	19	19	19	
Pyrite Content	Pearson	−0.768 (0.044)	0.571 (0.181)	0.656 (0.003)	0.661 (0.003)	0.681 (0.004)	−0.224 (0.357)	−0.149 (0.543)	−0.211 (0.385)	−0.458 (0.048)	1.000 (–)
	Spearman's rho	−0.612 (0.144)	0.612 (0.144)	0.448 (0.063)	0.414 (0.088)	0.602 (0.014)	−0.397 (0.092)	−0.269 (0.266)	−0.224 (0.356)	−0.389 (0.099)	1.000 (–)
	Number	7	7	18	18	16	19	19	19	19	20

Note: Data format: Correlation coefficient (significance).

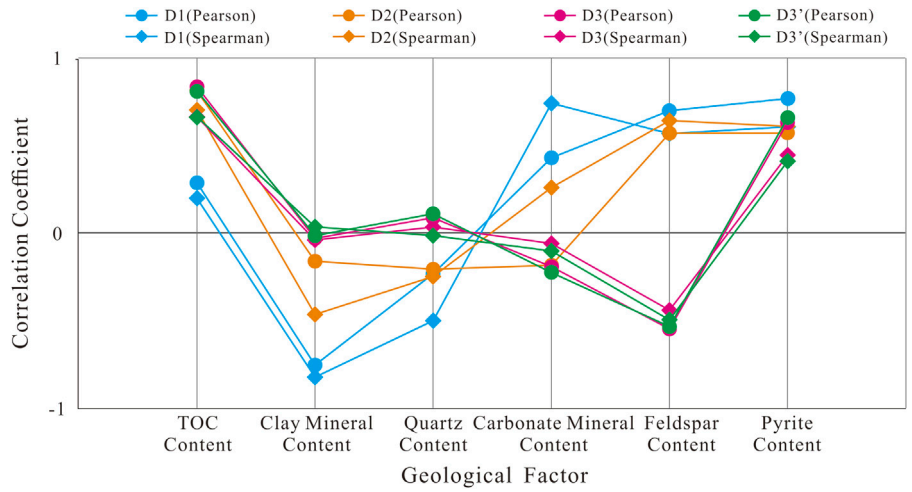

FIGURE 14
Main controlling factors analysis of multi-scale pore fractal dimension.

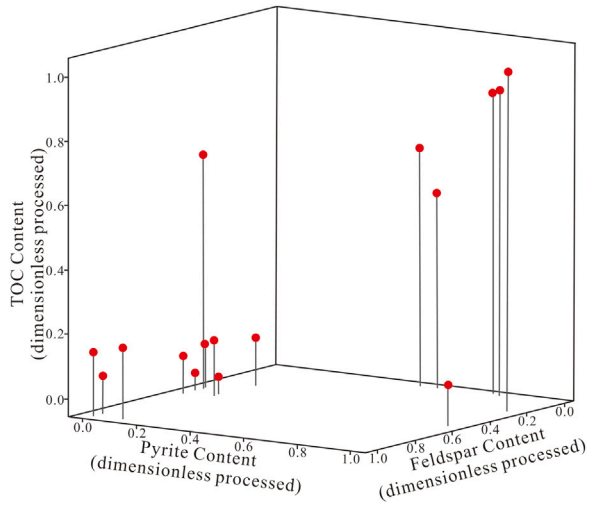

FIGURE 15
The correlation of TOC content-pyrite content—feldspar content.

Under similar organic matter maturity conditions, the development of organic pores is mainly controlled by the abundance of organic matter. The higher the abundance of organic matter, the more developed the organic pores and the larger D3 results. Further studies show that shale with low feldspar content and high pyrite content has the best organic matter abundance conditions (Figure 15). D3 has a significant negative and positive correlation with feldspar and pyrite content, respectively. This is because pyrite indicates a reducing environment conducive to preserving organic matter (Bond and Wignall, 2010; Kaplan et al., 2012; Zhang et al., 2013; Ma et al., 2016; Li et al., 2018), while feldspar is mainly terrigenous debris. Clastic rocks with high feldspar content have low compositional maturity and are affected by terrestrial sources, which are generally not conducive to preserving organic matter.

In conclusion, the main control factors of the pore structure of the Longtan shales with different apertures are different. The content of brittle minerals and pyrite mainly controls the macropore structure. The higher the content of pyrite, the lower the content of clay minerals, the more complex the macropore structure. The main controlling factors of mesopore structure are similar to those of macropore. However, due to the increase in the proportion of organic pores in mesopores, the influence of organic matter abundance on mesopore structure is significantly increased, making the controlling mechanism more complicated. The mini-micropore structure is mainly controlled by the organic matter abundance. The higher the abundance of organic matter, the more complex the mini-micropore structure.

5.2 Correlations between gas content and fractal dimensions

The results show that the total gas content of shale has a non-significant positive correlation with D1, D2, D3, and D3′ (Table 2). There is almost no correlation between total gas content and fractal dimensions. This is because the quantity of gas maintained in the shale pores is jointly controlled by hydrocarbon generation, gas storage, and preservation conditions. Pore development positively impacts the gas content, but it is only one of the influencing factors

TABLE 2 The correlation analysis results of the gas content and the fractal dimensions.

		Total gas content	Desorption gas/Total gas	Maximum adsorption gas volume	D1	D2	D3	D3′
Total gas content	Pearson	1.000 (–)						
	Spearman's rho	1.000						
	Number	9						
Desorption gas/total gas	Pearson	0.305 (0.424)	1.000 (–)					
	Spearman's rho	0.383 (0.308)	1.000 (–)					
	Number	9	9					
Maximum adsorption gas volume	Pearson	—	—	1.000 (–)				
	Spearman's rho	—	—	1.000 (–)				
	Number	1	1	7				
D1	Pearson	0.312 (0.609)	0.872 (0.054)	−0.416 (0.727)	1.000 (–)			
	Spearman's rho	0.600 (0.285)	0.800 (0.104)	−0.500 (0.667)	1.000 (–)			
	Number	5	5	3	10			
D2	Pearson	0.074 (0.906)	0.859 (0.062)	−0.865 (0.335)	0.602 (0.065)	1.000 (–)		
	Spearman's rho	0.600 (0.285)	1.000 (-)	−0.500 (0.667)	0.721 (0.019)	1.000 (–)		
	Number	5	5	3	10	10		
D3	Pearson	0.348 (0.398)	0.583 (0.130)	0.886 (0.008)	0.151 (0.721)	0.118 (0.781)	1.000 (–)	
	Spearman's rho	0.286 (0.493)	0.238 (0.570)	0.595 (0.159)	0.167 (0.693)	0.167 (0.693)	1.000 (–)	
	Number	8	8	7	8	8	23	
D3′	Pearson	0.368 (0.370)	0.558 (0.150)	0.881 (0.009)	0.027 (0.949)	0.268 (0.521)	0.962 (0.000)	1.000 (–)
	Spearman's rho	0.238 (0.570)	0.381 (0.352)	0.595 (0.159)	0.048 (0.911)	0.262 (0.531)	0.922 (0.000)	1.000 (–)
	Number	8	8	7	8	8	23	23

Note: Data format: Correlation coefficient (significance).

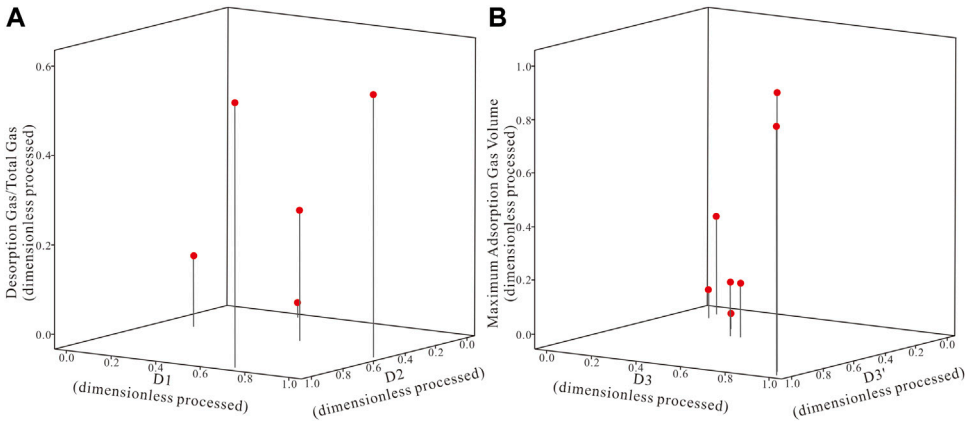

FIGURE 16
The correlation between gas content and fractal dimensions. [**(A)** the correlation of desorption gas/total gas–D1–D2; **(B)** the correlation of maximum adsorption gas volume–D3–D3′].

and cannot control the gas content. The ratio of desorption gas content to total gas content positively correlates with D1 and D2, and the correlation coefficient with D2 is slightly greater than D1 (Figure 16A), indicating that the pore structure of macro-mesopores is significant to the exploitability of shale gas resources in the Longtan Formation. For type B shale with developed and complex macro-mesopores, the proportion of gas that can be naturally produced in the total gas is large and easily exploitable.

The maximum adsorption gas volume is positively correlated with D3 and D3' (Figure 16B). Reflecting that mini-ve micropores are the main reservoir space of adsorbed gas, the development and structural complexity of mini-micropores is the controlling factor of the adsorption capacity of shale. Type III shale with the most complex mini-micropores has the best adsorption capacity, followed by type II shale, and type I rock has the worst adsorption capacity.

6 Conclusion

(1) The macropores of the Longtan shales in northwest Guizhou are mainly inorganic pores. The D1ranges from 2.8628 to 3.2057, with an average value of 3.0132. It is relatively large, and the macropore structure is relatively complex, accounting for a small proportion of the total pores. The proportion of inorganic pores in mesopores is still relatively high, but the proportion of organic pores gradually increases. The D2 ranges between 2.2125–2.3016, with an average of 2.2504. The complexity is medium, and the proportion in total pores is higher than that in macropores. Mini-micropores are mainly organic pores. The fractal dimension D3 is between 2.6709–2.8648, with an average value of 2.7489, and D3′ is between 2.6661–2.9256, with an average value of 2.7836. It is relatively large, with complex pore structures and rough surfaces, accounting for the highest proportion of the total pores.

(2) According to the mercury injection-ejection curve and mercury ejection efficiency, the Longtan shales can be divided into two types. In type A shales, mini-micropores are highly developed, followed by mesopores. The pore connectivity is medium, and D1 and D2 are relatively small. The proportion of mini-micropores in type B shales decreases, and the proportion of macro-mesopores increases. D1 and D2 are larger than type A shales, and the macro-mesopore structure is more complex than type A shales. At the same time, according to the N_2 adsorption-desorption curve, the Longtan shales can be divided into three types. The pores of the type I shale are mainly slit-shaped and wedge-shaped, and there are also some ink bottle-shaped pores. D3 and D3′ values are relatively low. The pores of the type II shale are mainly slit-shaped and wedge-shaped. D3 and D3′ are slightly larger than that of type I shales. The apertures of the type III shales are quite different, and micropores exist in the shale. D3 and D3′ values are both large, and the pore structure is the most complex.

(3) The macropore structure is jointly controlled by the brittle minerals and pyrite content. The shale with high brittle minerals and pyrite content has the highest D1 and the most complex macropore structure. The controlling mechanism of mesopore structure is more complicated because of the increase in the proportion of organic pores. The influence of organic matter abundance on mesopore structure is greater than that in macropore. The abundance of organic matter mainly controls the mini-micropore structure. The higher the organic matter abundance, the larger D3, and D3', and the more complex the mini-micropore structure.

(4) The macropore and mesopore structure greatly influence the proportion of desorption gas in shales. The larger D1 and D2, the more complex the macropores and mesopores, the higher the proportion of desorption gas, and the better the recoverability. The mini-micropore structure controls the maximum adsorbed gas volume of shale. The larger D3 and D3′, the more complex the mini-micropores, the larger the maximum adsorbed gas volume of shale, and the stronger the adsorption and gas storage capacity.

Data availability statement

The original contributions presented in the study are included in the article/Supplementary Material, further inquiries can be directed to the corresponding authors.

Author contributions

YH, JZ, and XT contributed to conception and design of the study. YH and PZ performed the statistical analysis. YH wrote the first draft of the manuscript. PZ, XT, and JY wrote sections of the manuscript. All authors contributed to manuscript revision, read, and approved the submitted version.

Funding

This work was supported by the Guizhou Education Department Youth Science and Technology Talents Growth Project (Grant Number QJH No. KY [2020]122), the Fund Program of the Science and Technology Department of Liupanshui City (Grant Numbers 52020-2018-03-03 and 52020-2019-05-03), and the Open Fund of Provincial and Ministerial Key Laboratory of China University of Geosciences (Beijing) (Grant Number. 20210113).

Conflict of interest

The authors declare that the research was conducted in the absence of any commercial or financial relationships that could be construed as a potential conflict of interest.

The reviewer ZX declared a shared affiliation with the authors YH, JZ, XT to the handling editor at the time of review.

Publisher's note

References

Bai, B., Zhu, R. K., Wu, S. T., Yang, W. J., Gelb, J., Gu, A., et al. (2013). Multi-scale method of Nano (Micro)-CT study on microscopic pore structure of tight sandstone of Yanchang Formation, Ordos Basin. *Petroleum Explor. Dev.* 40 (3), 354–358. doi:10.1016/S1876-3804(13)60042-7

Bond, D. P. G., and Wignall, P. B. (2010). Pyrite framboid study of marine permian-triassic boundary sections: A complex anoxic event and its relationship to contemporaneous mass extinction. *Geol. Soc. Am. Bull.* 122 (7-8), 1265–1279. doi:10.1130/B30042.1

Bureau of Geology and Mineral Exploration and Development Guizhou Province (1987). *Regional geology of Guizhou province*. Beijing: Geological Publishing House.B

Chalmers, G. R., and Bustin, R. M. (2008). Lower cretaceous gas shales in northeastern British Columbia, Part I: Geological controls on methane sorption capacity. *Bull. Can. petroleum Geol.* 56 (1), 1–21. doi:10.2113/gscpgbull.56.1.1

Chen, J., Zhou, G. Y., Zhao, X. L., and He, C. (2005). Overview of study methods of reservoir rock pore structure. *Special Oil Gas Reservoirs* 12 (4), 11–14+103.

Chen, S. B., Gong, Z., Li, X. Y., Wang, H. J., Wang, Y., and Zhang, Y. K. (2021). Pore structure and heterogeneity of shale gas reservoirs and its effect on gas storage capacity in the Qiongzhusi Formation. *Geosci. Front.* 12 (06), 1–17. doi:10.1016/j.gsf.2021.101244

Cheng, H., Jin, Z. K., Yu, W. R., Li, B. Q., Zhu, X. E., Chen, B., et al. (2022). Reservoir classification and evaluation based on fractal theory and factor analysis: A case study of the third member of the funing formation, qintong sag, subei basin. *Acta Sedimentol. Sin.*, 1–15. doi:10.14027/j.issn.1000-0550.2021.131

Clarkson, C. R., Solano, N., Bustin, R. M., Bustin, A. M. M., Chalmers, G. R. L., He, L., et al. (2012). Pore structure characterization of North American shale gas reservoirs using USANS/SANS, gas adsorption, and mercury intrusion. *Fuel* 103, 606–616. doi:10.1016/j.fuel.2012.06.119

Deng, H. Y., Sima, L. Q., Wu, W., Liu, F. L., Wang, X., Wang, C., et al. (2018). Fractal characteristics of pore structure and permeability calculation for tight sandstone reservoirs: A case of penglaizhen formation and shaximiao Formation in Western sichuan depression. *Lithol. Reserv.* 30 (6), 76–82. doi:10.12108/yxyqc.2018060

Deng, E. D., Zhang, Q., Jin, Z. J., Zhu, R. K., Yan, Z. H., Jiang, B. R., et al. (2022). Non-overmature equivalents confirmed a high initial hydrocarbon generation potential of the Permian Longtan Shale in southern China. *Int. J. Coal Geol.* 259, 1–17. doi:10.1016/j.coal.2022.104043

Feng, D. J. (2020). The characteristics and transformability of marine-continental transitional shale reservoirs of Longtan Formation in northwest Guizhou province. *J. Yangtze Univ. Nat. Sci. Ed.* 17 (3), 21–29+5. doi:10.16772/j.cnki.1673-1409.2020.03.004

Fu, X. H., Qin, Y., and Wei, C. T. (2007). *Coalbed methane geology*. Xuzhou: China University of Mining and Technology press.

Guo, X. J., Shen, Y. H., and He, S. (2015). Quantitative pore characterization and the relationship between pore distributions and organic matter in shale based on nano-CT image analysis: A case study for a lacustrine shale reservoir in the triassic chang 7 member, Ordos Basin, China. *J. Nat. Gas Sci. Eng.* 27(Part 3), 1630–1640. doi:10.1016/j.jngse.2015.10.033

Huang, Y. Q., Zhang, P., Zhang, J. C., Tang, X., Liu, C. W., and Yang, J. W. (2020). Fractal characteristics of pores in the longtan shales of Guizhou, southwest China. *Geofluids* 2020, 1–16. doi:10.1155/2020/8834758

Kaplan, I. R., Bird, K. J., and Tailleur, I. L. (2012). Source of molten elemental sulfur and hydrogen sulfide from the Inigok well, northern Alaska. *Am. Assoc. Pet. Geol. Bull.* 96 (2), 337–354. doi:10.1306/05021110202

Lai, J., Wang, G. W., Wang, S. N., Chai, Y., Wu, H., Zhang, Y. C., et al. (2013). Pore structure characteristics and controlling factors of 2nd and 4th member reservoirs in Upper Triassic Xujiahe Formation of Penglai area, central Sichuan Basin. *Geol. China* 40 (3), 927–938.

Li, D., Ou, C. H., Ma, Z. G., Jin, P. P., Ren, Y. J., and Zhao, Y. F. (2018). Pyrite-shale interaction in shale gas enrichment and development. *Geophys. Prospect. Petroleum* 57 (3), 332–343. doi:10.3969/j.issn.1000-1441.2018.03.002

Liu, K., and Ostadhassan, M. (2019). The impact of pore size distribution data presentation format on pore structure interpretation of shales. *Adv. Geo-Energy Res.* 3 (2), 187–197. doi:10.26804/ager.2019.02.08

Liu, H., Wu, S. H., Jiang, X. M., Wang, G. Z., Cao, Q. X., Qiu, P. H., et al. (2005). The configuration analysis of the adsorption isotherm of nitrogen in low temperature with the lignite char produced under fast pyrolysis. *J. China Coal Soc.* 30 (4), 507–510.

Liu, C., Ding, W. G., Zhang, J., Chen, X., Wu, P., Liu, X. Q., et al. (2021). Qualitative-quantitative multi scale characteristics of shale pore structure from Upper Paleozoic coal-bearing in Linxing area. *Coal Geol. Explor.* 49 (6), 46–57. doi:10.3969/j.issn.1001-1986.2021.06.005

Liu, M. H. (2020), Study on the composition, pore structure characterization of shale and their effects on adsorption characteristics. *Master's dissertation*. Chongqing: Chongqing University.

Loucks, R. G., and Reed, R. M. (2014). Scanning-electron-microscope petrographic evidence for distinguishing organic matter pores associated with depositional organic matter versus migrated organic matter in mudrocks. *GCAGS J.* 3 (2014), 51–60.

Loucks, R. G., Reed, R. M., Ruppel, S. C., and Hanmmes, U. (2012). Spectrum of pore types and networks in mudrocks and a descriptive classification for matrix-related mudrock pores. *Am. Assoc. Pet. Geol. Bull.* 96 (6), 1071–1098. doi:10.1306/08171111061

Ma, X. X., Zheng, J. J., Zheng, G. D., Xu, W., Qian, Y., Xia, Y. Q., et al. (2016). Influence of pyrite on hydrocarbon generation during pyrolysis of type-III kerogen. *Fuel* 167, 329–336. doi:10.1016/j.fuel.2015.11.069

Menger, K. (1928). *Dimensionstheorie*. Wiesbaden: Vieweg. doi:10.1007/978-3-663-16056-4_7

Pfeiferper, P., and Avnir, D. (1983). Chemistry non-integral dimensions between two and three. *J. Chem. Phys.* 79 (7), 3369–3558.

Qin, L., Wang, P., Lin, H. F., Zhao, P. X., Ma, C., and Shi, Y. (2020). Advanced characterization of pore structure of liquid nitrogen frozen coal using nitrogen adsorption and mercury intrusion methods. *J. Xi'an Univ. Sci. Technol.* 40 (6), 945–952. doi:10.13800/j.cnki.xakjdxxb.2020.0602

Ross, D. J. K., and Bustin, R. M. (2009). The importance of shale composition and pore structure upon gas storage potential of shale gas reservoirs. *Mar. Petroleum Geol.* 26 (6), 916–927. doi:10.1016/j.marpetgeo.2008.06.004

Rouquerol, J., Avnir, D., Fairbridge, C. W., Everett, D. H., Haynes, J. M., Pernicone, N., et al. (1994). Recommendations for the characterization of porous solids (Technical Report). *Pure Appl. Chem.* 66 (8), 1739–1758. doi:10.1351/pac199466081739

Shao, X. H., Pang, X. Q., Li, Q. W., Wang, P. W., Chen, D., Shen, W. B., et al. (2017). Pore structure and fractal characteristics of organic-rich shales: A case study of the lower silurian Longmaxi shales in the Sichuan Basin, SW China. *Mar. Petroleum Geol.* 80, 192–202. doi:10.1016/j.marpetgeo.2016.11.025

Su, Q. H. (2014). Formation condition and distribution prediction of shale gas of Longtan Formation in northwest Guizhou. Beijing: China University of Geosciences Beijing. Master's dissertation.

Su, Y. J. (2021). Mercury speciation in coal and transformation and stabilization in ultra-low emission coal-fired units. Beijing: North China Electric Power University. Doctoral dissertation.

Sun, L., Wang, X. Q., Jin, X., Li, J. M., and Wu, S. T. (2016). Three dimensional characterization and quantitative connectivity analysis of micro/nano pore space. *Petroleum Explor. Dev.* 43 (3), 537–546. doi:10.1016/s1876-3804(16)30063-5

Tang, R. Q., and Zeng, Y. H. (1994). The study on the retro-mercurometric efficiency of rocks. *Exp. Ppetroleum Geol.* 16 (1), 84–93.

Tian, H., Zhang, Y. C., Liu, S. B., and Zhang, H. (2012). Determination of organic-rich shale pore features by mercury injection and gas adsorption methods. *Acta Pet. Sin.* 33 (3), 419–427.

Tu, F. H., Tang, R. Q., Han, J. W., and Shen, P. P. (1983). Effect of sandstone pore structure on the efficiency of water drive. *Acta Pet. Sin.* 4 (2), 49–62. doi:10.7623/syxb198302009

Wood, D. A. (2021). Techniques used to calculate shale fractal dimensions involve uncertainties and imprecisions that require more careful consideration. *Adv. Geo-Energy Res.* 5 (2), 153–165. doi:10.46690/ager.2021.02.05

Xiao, X. M., Song, Z. G., Zhu, Y. M., Tian, H., and Yin, H. W. (2013). Summary of shale gas research in North American and revelations to shale gas exploration of lower Paleozoic strata in China south area. *J. China Coal Soc.* 38 (5), 721–727. doi:10.13225/j.cnki.jccs.2013.05.001

Xie, W. D., Wang, M., Wang, X. Q., Wang, Y. D., and Hu, C. Q. (2020). Nanopore structure and fractal characteristics of shale gas reservoirs: A case study of Longmaxi Formation in southeastern chongqing, China. *J. Nanosci. Nanotechnol.* 21 (1), 343–353. doi:10.1166/jnn.2021.18721

Xie, W. D., Wang, M., Wang, H., and Duan, H. Y. (2022). Multi-scale fractal characteristics of pores in transitional shale gas reservoir. *Nat. Gas. Geosci.* 33 (3), 451–460. doi:10.11764/j.issn.1672-1926.2021.06.006

Xoaotb, B. B., Song, S. Z., and Wang, Y. A. (1966). *Coal and gas outburst*. Beijing: China Industry Press.

Xu, S., Yang, Z. M., Wu, S. T., Wang, L., Wei, W., Yang, F., et al. (2022). Fractal analysis of pore structure differences between shale and sandstone based on the nitrogen adsorption method. *Nat. Resour. Res.* 31 (3), 1759–1773. doi:10.1007/s11053-022-10056-5

Xu, L. F. (2021). Accumulation model and gas-bearing evaluation of the shanxi Formation shale in fuxian area of Ordos Basin. Beijing: China University of Geosciences Beijing. Master's dissertation.

Yang, K., Lu, X. C., Xu, J. T., Yi, H. W., and Hu, W. X. (2013). Preliminary verification of distribution of shale common calculation methods of pore size based on has adsorption isotherm. *J. China Coal Soc.* 38 (5), 817–821. doi:10.13225/j.cnki.jccs.2013.05.017

Yang, F., Ning, Z. F., Kong, D. T., and Liu, H. Q. (2013). Pore structure of shales from high pressure mercury injection and nitrogen adsorption method. *Nat. Gas. Geosci.* 24 (3), 450–455.

Yang, F., Ning, Z. F., Wang, Q., Kong, D. T., Peng, K., and ang Xiao, L. F. (2014). Fractal characteristics of nanopore in shales. *Nat. Gas. Geosci.* 25 (4), 618–623. doi:10.11764/j.issn.1672-1926.2014.04.0618

Zhang, Q., Liu, H. L., Bai, W. H., and Lin, W. (2013). Shale gas content and its main controlling factors in Longmaxi Shales in southeastern Chongqing. *Nat. Gas. Ind.* 35 (5), 35–39. doi:10.3787/j.issn.1000-0976.2013.05.006

Zhang, J. P., Fan, T. L., Li, J., Zhang, J. C., Li, Y. F., Wu, Y., et al. (2015). Characterization of the lower cambrian shale in the northwestern Guizhou province, south China: Implications for shale-gas potential. *Energy fuels.* 29 (10), 6383–6393. doi:10.1021/acs.energyfuels.5b01732

Zhang, Q., Liu, R. H., Pang, Z. L., and Lin, W. (2016). Pore fractal characteristics of Taiyuan Formation shale in eastern uplift of Liaohe Depression. *Bull. Geol. Sci. Technol.* 35 (5), 77–82.

Zhang, P., Huang, Y. Q., Zhang, J. C., Liu, H. Y., and Yang, J. W. (2018). Fractal characteristics of the Longtan formation transitional shale in northwest Guizhou. *J. China Coal Soc.* 43 (6), 1580–1588. doi:10.13225/j.cnki.jccs.2018.4046

Zhang, P., Huang, Y. Q., Zhang, J. C., Li, B., Liu, H. Y., and Yang, J. W. (2020). Study on shale heterogeneity in Western hunan and hubei: A case study of the Longmaxi Formation in well Ld1. *Acta Geol. Sin.* 94 (5), 1568–1577. doi:10.19762/j.cnki.dizhixuebao.2020148

Zhang, J. C., Shi, M., Wang, D. S., Tong, Z. Z., Hou, X. D., Niu, J. L., et al. (2021). Fields and directions for shale gas exploration in China. *Nat. Gas. Ind.* 41 (8), 69–80. doi:10.3787/j.issn.1000-0976.2021.08.007

Zhu, R. K., Wu, S. T., Su, L., Cui, J. W., Mao, Z. G., and Zhang, X. X. (2016). Problems and future works of porous texture characterization of tight reservoirs in China. *Acta Pet. Sin.* 37 (11), 1323–1336. doi:10.7623/syxb20161101